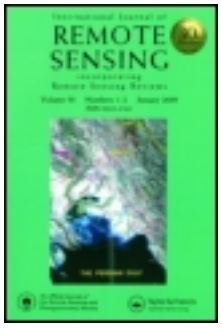

International Journal of Remote Sensing
Publication details, including instructions for authors and subscription information:
http://www.tandfonline.com/loi/tres20

Spectral signal to clutter and thermal noise properties of ocean wave imaging synthetic aperture radars

WERNER ALPERS [a] & KLAUS HASSELMANN [b]

[a] Institut für Geophysik, Universität Hamburg, and Max-Planck Institut für Meteorologie, Hamburg, F. R. Germany

[b] Max-Planck Institut für Meteorologie, Hamburg, F. R. Germany

Version of record first published: 27 Apr 2007.

To cite this article: WERNER ALPERS & KLAUS HASSELMANN (1982): Spectral signal to clutter and thermal noise properties of ocean wave imaging synthetic aperture radars, International Journal of Remote Sensing, 3:4, 423-446

To link to this article: http://dx.doi.org/10.1080/01431168208948413

INT. J. REMOTE SENSING, 1982, VOL. 3, NO. 4, 423–446

Spectral signal to clutter and thermal noise properties of ocean wave imaging synthetic aperture radars

WERNER ALPERS

Institut für Geophysik, Universität Hamburg, and Max-Planck Institut für Meteorologie, Hamburg, F. R. Germany

and KLAUS HASSELMANN

Max-Planck Institut für Meteorologie, Hamburg, F. R. Germany

(*Received 2 December 1981; revision received 11 August 1982*)

Abstract. The high wavenumber detection cut-off is determined above which the spectrum of ocean waves imaged by a synthetic aperture radar (SAR) is lost in the background noise spectrum consisting of the clutter noise associated with the Rayleigh statistics of the backscattering surface and the thermal noise originating in the SAR system itself. For given power, the maximum detection cut-off wavenumber is attained if the SAR resolution is chosen such that the clutter and noise spectra are equal at the cut-off wavenumber. Assuming a constant modulation transfer function relating the image modulation and wave slope spectra, the cut-off wavenumber is in this case proportional to $(\rho_a \rho_g)^{-1/2}$, where ρ_a and ρ_g represent the full bandwidth (single look) azimuthal and ground range resolutions, respectively. The same proportionality holds (but with a cut-off wavenumber increased by a factor $\sqrt{2}$) for a clutter limited cut-off, the normal operating condition of an SAR. To first order, incoherent multilook averaging has no influence on the signal-to-background detection cut-off wavenumber, provided the reduced Nyquist cut-off wavenumber resulting from the reduced multilook spatial resolution remains greater than the signal-to-background cut-off wavenumber. Estimates of the detection cut-off wavenumbers are given for the Seasat SAR and the SAR proposed for the European Remote Sensing Satellite ERS-1.

1. Introduction

It has been amply demonstrated in recent years that a synthetic aperture radar (SAR) flown on aircraft or spacecraft can image surface waves. However, it has also become evident that an SAR does not always image surface waves equally well. Cases have been recorded in which ocean waves measured by conventional sea truth instruments have not been detected by an SAR at all (Gonzales *et al.* 1979, Kasischke 1980). The deterioration of wave imagery can probably be attributed in part to the non-linearity of the SAR wave-imaging process, particularly for wind seas at low wind speeds (Alpers and Rufenach 1979, Swift and Wilson 1979, Valenzuela 1980, Rufenach and Alpers 1981, Alpers *et al.* 1981, Raney 1981). However, in other cases, such as low amplitude swell, or the short wavelength end of a wind wave spectrum, the wave image spectrum may simply be lost in the background noise spectrum. This consists of two contributions, the clutter spectrum, due to the random nature of the backscattering surface elements, and the normal thermal noise spectrum, originating in the SAR system itself. In the present paper we investigate this spectral signal-

to-background resolution limit, with particular emphasis on the short wavelength detection limit for wind seas. The determination of this limiting factor, and its dependence on SAR parameters, is clearly an important consideration for the optimization of an SAR designed for ocean wave detection.

The signal-to-background ratio for imaging radars is conventionally discussed in the image plane. The translation of these considerations into the spectral domain is basically straightforward for a backscattering surface, such as the sea surface, which may be regarded as a continuum of subresolution scale, statistically independent backscattering elements (facets). In this case the clutter contribution to the background spectrum is given by the constant (white) backscatter spectrum, modified at the high wavenumber end by the fall-off of the SAR impulse response function. The thermal noise spectrum has a similar structure, but with a different impulse response function (primarily because the noise, as opposed to the backscattered signal, does not pass through the antenna). In the relatively low wavenumber region of the spectrum relevant for surface waves, both impulse response functions can be regarded as approximately constant, and the net background spectrum is essentially white.

Ocean waves can be detected by an SAR if the superimposed spectrum of the wave-modulated image exceeds this white background level. For a simple wind-sea or swell spectrum consisting of a single peak one can then define low and high wavenumber detection cut-off wavenumbers on either side of the peak of the modulation spectrum where the modulation spectrum falls to the same level as the background spectrum (figure 1). The low wavenumber cut-off is of little concern, since the 'forward'

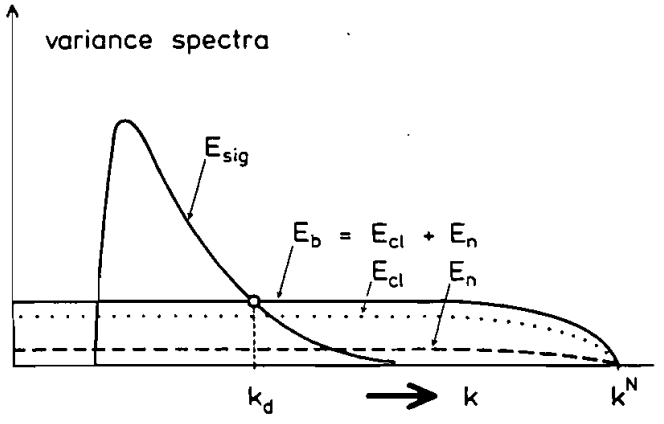

Figure 1. Signal spectrum E_{sig}, clutter spectrum E_{cl}, thermal noise spectrum E_n and total background noise spectrum $E_b = E_{cl} + E_n$ as functions of wavenumber $k = |\mathbf{k}|$ (schematic, for a given direction of the two-dimensional wavenumber $\mathbf{k}$). The detection wavenumber cut-off k_d is defined as the wavenumber for which $E_{sig} = E_b$. For $k_d \ll$ Nyquist wavenumber $k^N = (2\rho)^{-1}$, where ρ is the intrinsic SAR resolution in the direction considered, the spectra E_{cl}, E_n and E_b can be regarded as essentially white (wavenumbers are defined in units of cycles per unit length).

face of an ocean-wave spectrum is normally rather steep, both for wind seas and swell, so that there is relatively little information lost in the noise at wavenumbers below this cut-off. The high wavenumber detection cut-off k_d, however, is of more interest. This cut-off normally lies in the quasi-universal equilibrium region of the wind-sea

spectrum and determines the shortest waves which can be resolved in a given wind sea. Since the peak of a wind-sea spectrum moves towards higher wavenumbers with decreasing wind speed, the existence of a high wavenumber cut-off k_d implies that a wind-sea spectrum cannot be detected for wind speeds below a critical value for which the peak wavenumber becomes equal to k_d. For Seasat, the cut-off wavelength is of order 60 m and the associated critical wind speed 8 m/s^{-1}.

A SAR represents only one of various possible microwave techniques proposed to measure ocean waves. If the goal of the measurement is to determine the ocean-wave spectrum, there is in principle no need to use an imaging system, and one can consider more general 'Fourier transforming radars' which yield the spectral information of a scene directly. Dual frequency or Δk-radars, operated in either real or synthetic aperture modes, represent special examples of such radars (Plant 1977, Alpers and Hasselmann 1978, Jackson 1980). The direct extraction of spectral information from an SAR without the intermediate step of forming an image also corresponds to this approach (Hasselmann 1980, Martin 1981). A more general analysis of the signal-to-background properties of non-imaging, Fourier transforming radars is given in Hasselmann and Alpers (1983). The present paper may be considered as a special case of the general analysis, expressed in the more familiar terminology of imaging radars.

Qualitatively, the relations derived in this paper are consistent with the statistics on the detectability of ocean waves in Seasat SAR images summarized by Kasischke (1980). A more quantitative test of the analysis, however, requires simultaneous measurements of sea truth and the backscatter modulation transfer functions which determine the modulation depth of the SAR wave image. It is expected that this information will become available through the set of SAR flights, microwave tower experiments and ground truth measurements conducted during the Marine Remote Sensing Experiment (MARSEN). The advent of this data set provided, in fact, one of the motivations for the present study.

In §2 we briefly review the basic concepts of SAR imaging of a moving random sea surface. The modulation and clutter spectra of the sea surface are derived in §3 by elementary scaling arguments, ignoring details of the SAR system response functions and finite-resolution spectral filters. A more complete discussion is given in Appendix A. The signal-to-background ratio for a background spectrum consisting of superimposed clutter and thermal noise components, the dependence of the detection cut-off wavenumber on the SAR parameters, and the optimization of an SAR with respect to the detection cut-off wavenumber, are considered in §4. Details are again deferred to Appendices B and C, while in Appendix D the basic results derived under the assumption of single-look processing are shown to apply also for multilook processing. In §5, finally, some numerical estimates are given for the Seasat SAR and the SAR proposed for the first European remote sensing satellite ERS-1.

2. SAR imaging of a moving random sea surface

Satellite and airborne synthetic aperture radars normally operate at angles of incidence between 20° and 70° for which the microwave return from the sea surface is predominantly due to Bragg backscattering from short surface ripples. Longer waves are seen by the radar because they modulate the backscattering due to the short surface ripples. The modulation can be described in terms of a two-scale model in which the sea surface is represented as a superposition of short Bragg backscattering ripples and longer gravity waves. The Bragg scattering theory is applied locally in a

reference system lying in tangent planes ('facets') of the long waves and moving with the local long-wave orbital velocity (Bass *et al.* 1968, Wright 1968, Keller and Wright 1975, Alpers and Hasselmann 1978).

Three processes contribute to long-wave imaging:

(1) The modulation of the energy of the short Bragg scattering ripples through interactions between the ripple waves and the long gravity waves (hydrodynamic interactions).
(2) The changes, through the long wave slope, in the effective angle of incidence relative to the local facet normal; this modifies the radar return by changing both the Bragg backscattering coefficient and the resonant Bragg wavenumber (electromagnetic interactions).
(3) The temporal variations of the facet parameters (facet position, direction of facet normal) and the Bragg backscattering coefficients of the facets during the finite integration time in which the SAR sees a facet (motion effects).

The first two processes are important for both real aperture and synthetic aperture radars, while the third process affects only synthetic aperture radars.

The motion effects can be evaluated analytically by noting that the SAR integration time (typically 0·1–3 s) is generally short compared with both the period of the long waves ($\sim$ 8–16 s), and the hydrodynamic interaction time of the backscattering ripples (typically at least several seconds). Thus the temporal variations of the facet parameters and the complex backscattering coefficient can be expanded in a Taylor series with respect to the integration time. The dominant terms in the expansion are found to arise from the slant-range components of the facet velocity and acceleration (Alpers and Rufenach 1979, Swift and Wilson 1979, Valenzuela 1980, Alpers *et al.* 1981). The first term gives rise to a displacement, and the second term to a stretching (blurring, defocusing) of the facet in azimuth direction.

For all three imaging processes, the backscattering moving sea surface may be replaced for the purposes of the signal-to-background analysis of the present paper by an equivalent frozen sea surface. This is obtained by simply mapping the original moving backscattering facets into an equivalent frozen ensemble of displaced and stretched backscattering elements. The facet stretching through azimuthal defocusing does not affect the correlation scale or the statistics of the backscattering elements even when the stretching becomes comparable to the azimuthal SAR resolution. This follows from analogy with pulse decompression, which also has no effect on the spectral statistics of the backscattering elements (Raney 1981).

In the linear-imaging regime, the relation between the SAR image (signal) spectrum $E_{sig}(\mathbf{k})$, representing the variance spectrum of the modulated cross-section distribution of the equivalent backscattering frozen surface, and the surface wave spectrum $E_w(\mathbf{k})$ (defined, in contrast to the usual definition in surface wave theory, as the symmetric surface elevation variance spectrum, without distinction between the two propagation directions associated with a given $\mathbf{k}$) can be expressed in the form

$$E_{sig}(\mathbf{k}) = |M|^2 \bar{\sigma}_0^2 (2\pi k)^2 E_w(\mathbf{k}) \tag{1}$$

where the complex non-dimensional transfer function $M(\mathbf{k})$ represents the ratio, for each Fourier component, of the amplitude of the relative cross-section modulation to the amplitude of the sea surface slope. In equation (1), as throughout this paper, we define wavenumbers as spatial 'Hertz' in units of cycles per unit length, rather than the more usual definition of radians per unit length. (This is convenient for removing

factors of 2π and maintaining Fourier transform symmetry in the convolution algebra required in the following sections.)

The net transfer function $M(\mathbf{k})$ is given by the superposition of the three individual complex transfer functions of the three separate imaging processes. Theoretical estimates (Keller and Wright 1975, Alpers and Hasselmann 1978) yield values of $|M|$ of order 3–10 and existing measurements, although strongly scattered, mostly lie in this range (Wright *et al.* 1980).

Inserting into equation (1) Phillips' wind-sea spectrum (Phillips 1977)

$$E_w(\mathbf{k}) = \frac{\alpha \cos^2 \phi}{(2\pi)^3 k^4} \qquad (k \gtrsim k_p) \tag{2}$$

where α is the Phillips constant and ϕ the angle between the wave and wind direction, yields for the modulation image spectrum

$$E_{sig}(\mathbf{k}) = (2\pi)^{-1} \alpha \bar{\sigma}_0^2 |M|^2 k^{-2} \cos^2 \phi \tag{3}$$

Phillips spectrum and the form (3) apply for wavenumbers greater than the peak wavenumber k_p, which is a function of wind speed and the state of development of the wind sea. For a fully developed spectrum, $\alpha \approx 0{\cdot}008$. Somewhat higher values of α are found for underdeveloped wind seas.

Note that this equation is valid only if the SAR imaging of the ocean surface can be described by a linear modulation transfer function. For certain ranges of SAR and ocean-wave parameters the SAR imaging mechanism may become non-linear due to the motion of the ocean surface (Alpers *et al.* 1981). In this case the evaluation of $E_{sig}(\mathbf{k})$ requires a more refined analysis.

For later numerical estimates, we shall normally assume that $|M| = \text{const.}$ in equation (3). Taking the rather conservative value $|M| = 4$ and the fully developed value $\alpha = 0{\cdot}008$, equation (3) yields

$$E_{sig}(\mathbf{k}) = 0{\cdot}02 \bar{\sigma}_0^2 k^{-2} \cos^2 \phi \tag{4}$$

Comparisons of SAR images with sea truth wave spectra (McLeish *et al.* 1980, Vesecky and Stewart 1982) suggest that in some cases the square modulus of the net imaging transfer function may be better approximated by an inverse wavenumber dependence $|M|^2 \approx |M_0|^2 \cdot k_0/k$ (with constant M_0, k_0) rather than by a constant. In this case (3) becomes

$$E'_{sig}(\mathbf{k}) = (2\pi)^{-1} \alpha \bar{\sigma}_0^2 |M_0|^2 k_0 k^{-3} \cos^2 \phi \tag{5}$$

Equations (4) and (5) do not differ significantly in order of magnitude and general spectral shape, but the different k exponents yield different dependencies for the signal to-background detection cut-off wavenumber on the SAR resolution cell area, computed later in §4, equations (29) and (30).

3. Statistical description of backscattering and the clutter spectrum

To a good approximation, the SAR image obtained for a moving sea surface can be reduced to the image of an equivalent time-independent ('frozen') surface whose complex backscattering coefficient $r(\mathbf{x})$ can be represented as the product

$$r(\mathbf{x}) = w(\mathbf{x}) m^{1/2}(\mathbf{x}) \tag{6}$$

of a random, statistically homogeneous, complex white noise process $w(\mathbf{x})$, which

represents the backscattered return due to uniformly distributed, small-scale (Bragg scattering) ripples, and a slowly varying function $m^{1/2}(\mathbf{x})$, which describes the modulation of this return by the long gravity waves.

The covariance functions of $w(\mathbf{x})$ and $r(\mathbf{x})$ are given by

$$\langle w^*(\mathbf{x}+\mathbf{x}')w(\mathbf{x})\rangle = \delta(\mathbf{x}')\bar{\sigma}_0 \tag{7}$$

$$\langle r^*(\mathbf{x}+\mathbf{x}')r(\mathbf{x})\rangle = \delta(\mathbf{x}')\sigma_0(\mathbf{x}) \tag{8}$$

where

$$\sigma_0(\mathbf{x}) = m(\mathbf{x})\bar{\sigma}_0 \tag{9}$$

represents the spatially dependent local backscattering cross-section per unit (horizontal) surface area, the cornered parentheses denote local ensemble averages over the small scale backscattering ripples, and the mean bars denote ensemble averages (in practice: large scale spatial averages) over different realizations of the large-scale wave field.

In the following section we shall consider also mean values defined with respect to an ensemble of thermal noise realizations. Where necessary, we shall distinguish between these three forms of averaging by referring to clutter-averaged, spatially-averaged and noise-averaged quantities.

From (8) it follows that the clutter-mean backscatter power reflectivity of an infinitesimal surface area element δA is

$$\langle |(\textstyle\int_{\delta A} r(\mathbf{x})\, d\mathbf{x})|^2\rangle = \sigma_0(\mathbf{x})\delta A \tag{10}$$

as required for the definition $\sigma_0(\mathbf{x})$. The representation of the small-scale backscattering coefficient $w(\mathbf{x})$ as a zero correlation-scale random process is standard and valid provided the correlation scale of the backscattering elements is small compared with the SAR resolution, which is normally well satisfied.

Since the SAR processor is linear, the complex image $c(\mathbf{x})$ produced by the SAR may be represented generally as a convolution.

$$c = r * s \tag{11}$$

where $s(\mathbf{x})$ denotes the SAR (signal) impulse response function.

The clutter-averaged real image $\langle I(\mathbf{x})\rangle$ is obtained by forming the square modulus of the complex image (11) and averaging over the ensemble of small scale scatters. From equations (6)–(11) we obtain

$$\langle I(\mathbf{x})\rangle = \langle |c(\mathbf{x})|^2\rangle = \sigma_0(\mathbf{x}) * |s|^2 \tag{12}$$

In this section we consider only single-look image processing. A single-look image represents a single realization of the backscattering sea surface over which the SAR passes. Thus the image is formed without clutter averaging, and consists of a superposition

$$I(\mathbf{x}) = \langle I(\mathbf{x})\rangle + I'(\mathbf{x}) \tag{13}$$

of the mean image, as given by (12), and a clutter or speckle term $I'(\mathbf{x})$.

The variance spectrum of the image will accordingly consist of the variance spectrum $E_{sig}(\mathbf{k})$ of the mean, clutter-averaged image (the signal) and the clutter spectrum $E_{cl}(\mathbf{k})$. The clutter contribution is derived in detail in Appendix A. The principal features of the clutter spectrum, however, can be understood very simply in

terms of an elementary scaling analysis of SAR imaging which retains the basic argument while avoiding details of the response and filter functions and the attendant convolution algebra required for a rigorous treatment.

The SAR image resolution is determined by the aximuthal and ground range widths ρ_a, ρ_g, respectively, of the square modulus of $|s|^2$ in equation (12). For the present elementary scaling analysis we assume that the SAR impulse response function may be regarded as a two-dimensional box-car function which is constant $=(\rho_a\rho_g)^{-1/2}$ in the rectangle $|x_a| \leqslant \rho_a/2$, $|x_g| \leqslant \rho_g/2$ and zero elsewhere. We consider also a discretized SAR image with the discretization intervals $\Delta x_a = \rho_a$, $\Delta x_g = \rho_g$. In this case equation (12) yields

$$\langle I(\mathbf{x})\rangle = \sigma_0(\mathbf{x}) \tag{14}$$

at the discrete grid points $\mathbf{x}$.

The normalization of s chosen here in which the image is expressed in units of the cross-section is natural for the discussion of the clutter contamination, and also the thermal noise in the next section, in the framework of the present scaling analysis. However, this normalization is less convenient for the detailed analysis presented in Appendices A and C and is therefore replaced there by a normalization in which I is referred to the input power at the SAR receiver.

For a box-car response function, the complex numbers c for different pixels are statistically uncorrelated. Moreover, since they are formed by integrating over a white process, it follows from the Central Limit Theorem that they represent complex Gaussian variables, for which the fourth and second moments are related through $\langle(|c|^2 - \langle|c|^2\rangle)^2\rangle = \langle|c|^2\rangle^2$. For the discretized image $I(x) = |c|^2 = \langle I\rangle + I'$ this yields

$$\langle I'(x)^2\rangle = \langle I(x)\rangle^2 = \sigma_0^2(\mathbf{x}) = m^2(\mathbf{x})\bar{\sigma}_0^2 \tag{15}$$

For a non-modulated image, $m = 1$, consisting only of clutter noise, $I'(\mathbf{x}) = I_0'(\mathbf{x})$ represents a statistically homogeneous, discrete, zero-correlation scale (i.e. white noise) process. Thus the clutter variance spectrum $E_{cl}^0(k_a, k_g)$ is constant up to the Nyquist cut-off wavenumbers $k_a^N = (2\rho_a)^{-1}$, $k_g^N = (2\rho_g)^{-1}$. We remind that wavenumbers are defined here, as throughout, in units of cycles per length.

The constant follows from the normalization (for a two-sided variance spectrum)

$$\int_{-k_a^N}^{k_a^N}\int_{-k_g^N}^{k_g^N} E_{cl}^0(\mathbf{k})\, dk_a\, dk_g = \langle I_0'^2\rangle$$

which yields

$$E_{cl}^0(\mathbf{k}) = \begin{cases} \bar{\sigma}_0^2\,\delta A & \text{for } |k_a| < k_a^N, |k_g| < k_g^N \\ 0 & \text{otherwise} \end{cases} \tag{16}$$

where $\delta A = \rho_a\rho_g$ denotes the area of the resolution cell (pixel).

In the case of a modulated image, $m \neq 1$, the clutter contamination may be written as

$$I' = I_0' \cdot m = I_0' + I_0' \cdot m' \tag{17}$$

where $m' = m - 1$ denotes the deviation of the modulation function m from its mean value of unity. Since m' and I_0' are statistically independent, the variance spectrum of the modulated clutter is given by (Jenkins and Watts 1968)

$$E_{cl} = E_{cl}^0 + E_{cl}^0 * E_{m'} \tag{18}$$

where $E_{m'}(\mathbf{k})$ represents the variance spectrum of m'. For a white spectrum E_{cl}^0 given by (16), equation (18) yields again a constant white-noise spectrum,

$$E_{cl}=\overline{m^2}E_{cl}^0=\begin{cases}\overline{\sigma_0^2}\cdot\rho_a\cdot\rho_g & \text{for } |k_a|<k_a^N, |k_g|<k_g^N\\ 0 & \text{otherwise}\end{cases} \tag{19}$$

Equation (19) may also be derived directly by noting that, if I_0' is a white noise process with

$$\langle I_0'(\mathbf{x}_1)I_0'(\mathbf{x}_2)\rangle=\delta_{x_1x_2}\bar{\sigma}_0^2$$

then the modulated process $I'=m\cdot I_0'$ represents a statistically homogeneous, white noise process with respect to a statistical ensemble including both the long waves and the Bragg scattering ripples. Formally, the clutter ensemble may be incorporated simply in the long-wave ensemble, since each realization of the long waves may be assumed to be associated with an independent realization of the small-scale scatterers. Thus one obtains

$$\langle I'(\mathbf{x}_1)I'(\mathbf{x}_2)\rangle\equiv I'(\mathbf{x}_1)I'(\mathbf{x}_2)=\delta_{x_1x_2}\overline{m^2}\bar{\sigma}_0^2=\delta_{x_1x_2}\overline{\sigma_0^2} \tag{20}$$

which yields the spectrum (19).

The complete variance spectrum $E(\mathbf{k})$ of the image consists of a superposition of the clutter spectrum (19) and the variance spectrum of the (clutter-averaged) mean wave image $\langle I(x)\rangle$, which we refer to simply as the signal spectrum $E_{sig}(\mathbf{k})=\bar{\sigma}_0^4E_m(\mathbf{k})$ (see figure 1),

$$E(\mathbf{k})=E_{sig}(\mathbf{k})+E_{cl}(\mathbf{k}) \tag{21}$$

In general, $E_{sig}(\mathbf{k})$ falls off towards high wavenumbers and will therefore disappear in the clutter spectrum beyond some cut-off wavenumber k_d.

A more detailed analysis of the image and clutter spectrum, taking into consideration the form of the SAR impulse response function and the finite extent of the scene, Appendix A, yields in place of the relation (19)

$$E_{cl}=\bar{\sigma}_0^2\cdot(|\hat{s}|^2*|\widehat{s^*}|^2*|\hat{H}|^2) \tag{22}$$

while the signal spectrum is given by

$$E_{sig}=[E_\sigma^\infty\cdot(\widehat{|s|^2})^2]*|\hat{H}|^2 \tag{23}$$

Here H denotes the fading function occurring in the computation of the finite resolution Fourier components of a finite scene, s is the impulse response function defined in equation (11), and $E_\sigma^\infty(\mathbf{k})$ is the asymptotic, infinite resolution, continuous variance spectrum of the cross-section field $\sigma_0(\mathbf{x})$. The circumflex $\hat{}$ denotes the Fourier transform. Equation (21) applies for small modulation levels for which $E_{cl}\approx E_{cl}^0$ (the general expression for arbitrary modulation levels is given in Appendix A, equations (A 16) and (A 17)).

The main difference between the approximate and exact relations is a more gradual roll-off of the exact clutter spectrum (and signal spectrum) as one approaches the Nyquist cut-off wavenumbers k_a^N, k_g^N (with an associated modification of the clutter energy level also in the white region of the spectrum at wavenumbers small compared with $\mathbf{k}^N$).

4. The spectral signal-to-background ratio

The total background contamination of an SAR image consists of both random

clutter fluctuations, and the contribution from thermal noise within the SAR system. Since thermal noise also originates from a white noise source, the net background variance spectrum E_b can be represented within the framework of the elementary scaling analysis of the last section by the sum

$$E_b = E_{cl} + E_n \tag{24}$$

of the clutter spectrum E_{cl} and the thermal noise spectrum E_n, both of which may be regarded as approximately constant up to the Nyquist cut-off wavenumbers. The spectral thermal noise level can be expressed in cross-section units in a form analogous to (19),

$$E_n = (\sigma_0^{ne})^2 \rho_a \cdot \rho_g \tag{25}$$

where the 'noise equivalent cross-section' σ_0^{ne} (see Appendix C) is given by

$$\sigma_0^{ne} = \frac{kT_n}{\bar{W}_e} \frac{2(4\pi)^3 r^3}{\lambda_0^3 G_a^2 \eta^2} \frac{V}{\rho_g} \tag{26}$$

Here $\bar{W}_e$ denotes the mean power, G_a the antenna gain, η the antenna efficiency factor, ρ_g the ground range solution, V the platform velocity, λ_0 the radar wavelength, T_n the system noise temperature and k is Boltzmann's constant.

A more detailed analysis, allowing for the form of the impulse response function s_n of the SAR with respect to the thermal noise input, yields (see Appendix C, equation (C 14))

$$E_n = (kT_n)^2 (|\hat{s}_n|^2 * |\widehat{s_n^*}|^2 * |\hat{H}|^2) \tag{27}$$

Equation (27) has the same basic structure as the corresponding exact expression (22) for the clutter spectrum. However, it is important to note that the thermal noise impulse response function s_n in equation (27) differs from the signal impulse response function s appearing in (23). The latter represents the SAR response to an infinitesimal surface scatterer and therefore involves properties of the entire SAR system, including the antenna pattern and emitted pulse form, whereas the thermal noise impulse response function depends only on properties of the SAR receiver and processor. Because of this difference in the signal and noise impulse response functions, it is not convenient to use equivalent cross-section units, as in the approximate scaling relation (25), for the exact expression of the thermal noise spectrum. Equation (27) is therefore expressed, as the analogous exact equation (22) for the clutter spectrum in units of received power (see Appendixes A and C).

The signal-to-background detection cut-off wavenumber k_d is defined as the wavenumber for which the signal spectrum has decreased to the background noise level,

$$E_{sig}(k_d) = E_b(k_d) \tag{28}$$

Inserting equations (3) and (5) into equation (28) yields

$$k_d = \left(\frac{\alpha}{2\pi}\right)^{1/2} \bar{\sigma}_0 |M \cos\phi| (E_b)^{-1/2} \tag{29}$$

for $|M| = \text{const.}$ and

$$k_d = \left(\frac{\alpha}{2\pi}\right)^{1/3} (\bar{\sigma}_0^2 |M_0 \cos\phi|^2 k_0)^{1/3} (E_b)^{-1/3} \tag{30}$$

for $|M| = M_0 (k_0/k)^{1/2}$, respectively.

To optimize wave detection, the cut-off wavenumber k_d should be maximized by minimizing the background spectrum. The optimal solution will depend in general on the side conditions imposed on the SAR operation. We assume in the following that the mean emitted power, the mean incidence angle, the platform velocity and the wavelength of the SAR are prescribed, and that the SAR is operated at the maximal swath width attainable within the ambiguity limits set by the azimuthal resolution.

Under these conditions, the swath width is approximately proportional to the azimuthal resolution scale ρ_a. This implies that the area of the antenna and therefore the antenna gain G_a and the thermal noise spectrum, equation (25) and (26), are independent of azimuthal resolution. The azimuthal resolution still enters the clutter spectrum, equation (19). However, the choice of ρ_a reduces then essentially to a trade-off between the level of the clutter spectrum and the swath width (and also the bit rate). Since this involves considerations beyond the signal-to-background analysis of the present study, we regard here the swath width and azimuthal resolution ρ_a as given, together with the other externally prescribed SAR parameters.

The only remaining free parameter is then the ground range resolution ρ_g. The clutter and noise spectra exhibit opposite dependencies on ρ_g, $E_{cl} = A_{cl}\rho_g$, $E_n = A_n\rho_g^{-1}$, where A_{cl} (for a given sea surface) and A_n are constants. The minimum value of the background spectrum

$$E_b = A_{cl}\rho_g + A_n\rho_g^{-1} \tag{31}$$

is attained when

$$\frac{\partial E_b}{\partial \rho_g} = 0 = \frac{1}{\rho_g}(A_c\rho_g - A_n\rho_g^{-1}) = 0 \tag{32}$$

i.e. when the clutter and noise spectra are equal,

$$E_{cl} = E_n$$

This is equivalent to the condition that the noise equivalent cross-section σ_0^{ne} is equal to the mean cross-section σ_0, since, as the r.m.s. clutter per pixel is equal to the mean return power, equation (15), it follows that for $\sigma_0^{ne} = \sigma_0$ the clutter and thermal noise contributions per pixel, and therefore the associated white noise spectra, are also equal.

The mean cross-section entering as factor in the clutter spectrum E_{cl} (equation (19)) is not constant, but increases with wind speed. It is therefore not possible to design an SAR to satisfy the optimal condition (32) under all wind conditions. If the SAR satisfies (32) for some prescribed (low) wind speed, the detection cut-off will be thermal noise limited for lower wind speeds and clutter limited for higher wind speeds, since the cross-section σ_0 increases with increasing wind speed. Normally, a SAR will need to be designed with sufficient system margin to ensure that the SAR is operated in the clutter-limited regime for all except very low wind speeds. For fixed SAR system parameters, the dependence of the detection cut-off wavenumber on σ_0 for a constant modulation transfer function M (equation (29)) is given by

$$k_d = k_d^{opt}\sqrt{2}\sigma_0[(\sigma_0^{ne})^2 + \sigma_0^2]^{-1/2} \tag{33}$$

For fixed spatial resolution, the detection cut-off wavenumber in the clutter-limited regime is greater than the optimal cut-off for a clutter-to-noise ratio of unity by a factor $\sqrt{2}$, independent of the cross-section, while the cut-off increases linearly with the cross-section in the thermal-noise-limited segime (figure 2). (Note that the

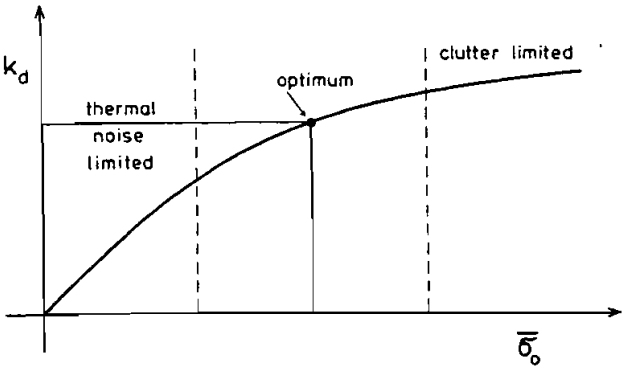

Figure 2. Cross-section dependence of the detection cut-off wavenumber k_d, equation (34), for a fixed SAR parameter.

inequality $k_d^{cl} > k_d^{opt}$ implies higher power for given σ_0 in the clutter-limited regime and therefore does not contradict the fact that the k_d^{opt} corresponds to the optimal solution for given power.)

Insertion of $E_b = E_{cl}$ (equation (19)), $E_b = E_{cl} + E_n$ with $E_n = E_{cl}$ (equation (19)), and $E_b = E_n$ (equation (25)) yields the cut-off wavenumbers in the clutter-limited, the optimal, and the thermal-noise-limited regimes, respectively

$$k_d^{cl} = \left(\frac{\alpha}{2\pi}\right)^{1/2} \left(\frac{\bar{\sigma}_0^2}{\sigma_0^2}\right)^{1/2} |M \cos\phi| (\rho_a \rho_g)^{-1/2} \tag{34}$$

$$k_d^{opt} = \frac{1}{\sqrt{2}} k_d^{cl} \tag{35}$$

$$k_d^{n} = \left(\frac{\alpha}{2\pi}\right)^{1/2} |M \cos\phi| \left(\frac{\bar{\sigma}_0}{\sigma_0^{ne}}\right) (\rho_a \rho_g)^{1/2} \tag{36}$$

A graphical method for determining the cut-off wavenumber is shown in figure 3. The curves $E_b = E_{cl} + E_n$ are plotted as functions of the Nyquist wavenumber $k_N^g = (2\rho_g)^{-1}$. The thermal-noise branches of the curves are parameterized by the ratio of the average power $\overline{W_e}$ to the system noise temperature T_n. On the left-hand side of the figure, the cross-section modulation spectrum E_{sig} is plotted as a function of k (for a given wave direction ϕ). The maximal detection cut-off for a given power-to-noise temperature ratio is evidently obtained at the resolution ρ_g^{opt} for which $E_{cl} = E_n$. Also shown are the three detection cut-off wavenumbers k_d^{cl}, k_d^{n}, k_d^{opt} at a given resolution and three different power-temperature ratios corresponding to the cases of a clutter-limited, noise-limited and optimally operated SAR.

Figure 4 shows the clutter-limited direction cut-off wavelength $\lambda_d^{cl} = 1/k_d^{cl}$ as a function of ρ_g, ρ_a and $|M \cos\phi|$. (Note again that wavenumbers are given in cycles rather than radians per unit length.)

5. Estimates of signal-to-background cut-off wavenumber for Seasat and ERS-1

We now apply the results of §4 to estimate the spectral signal-to-background properties of the SAR flown on Seasat-1 (Jordan 1980) and the SAR proposed in the payload for the first European Remote Sensing Satellite (ERS-1) scheduled for launch in 1987.

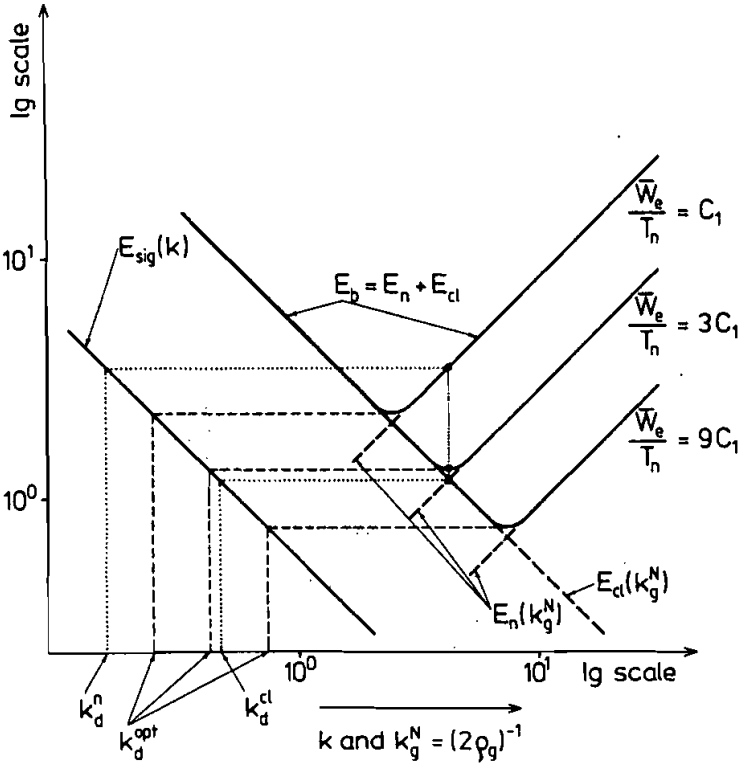

Figure 3. Signal spectrum $E_{sig}(\mathbf{k})$, as a function of wavenumber and spectral noise levels E_n, E_{cl} and E_b, as functions of Nyquist wavenumber $k_N^g = (2\rho_g)^{-1}$ with associated detection cut-off wavenumber k_d.

5.1. *Seasat SAR*

The calculated noise-equivalent radar cross-section σ_0^{ne} for Seasat SAR is $-28{\cdot}6$ db (Beal *et al.* 1977). The value follows from equation (26) on inserting the parameters $\bar{W}_e = 1000$ W, $T_n = 690$ K, $r = 850$ km, $\lambda_0 = 0{\cdot}23$ m (L-band), $V = 7{\cdot}4$ km s^{-1}, $\rho_g = 25$ m, $G_a = 5500$, and $\eta = 50$ per cent. However, preliminary analysis of measurements with the Seasat SAR indicate that the true σ_0^{ne} is -21 ± 5 db (Jordan 1980). This value is still considerably smaller than typical radar cross-sections σ_0 associated with L-band sea clutter at 20° incidence angle, which vary from a minimum of -16 db (low wind speeds, cross-wind direction) to a maximum of -9 db. Thus the Seasat SAR was always clutter limited over the ocean. Insertion of the Seasat one-look resolutions ($\rho_g = 25$ m $\rho_a = 6{\cdot}25$ m) into equation (34) and assuming $\overline{\sigma_0^2} \approx \bar{\sigma}_0^2$ yields

$$(\lambda_d^{cl})_{Seasat} \approx \frac{360}{|M \cos \phi|} \tag{37}$$

This cut-off wavelength is plotted in figure 5 as a function of $|M \cos \phi|$.

5.2 *Proposed ERS-1 SAR*

The parameters presently proposed for the SAR mode of the Active Microwave Instrument (AMI) to be flown onboard ERS-1 are (DORNIER 1980): $\lambda_0 = 5{\cdot}5$ cm (C-

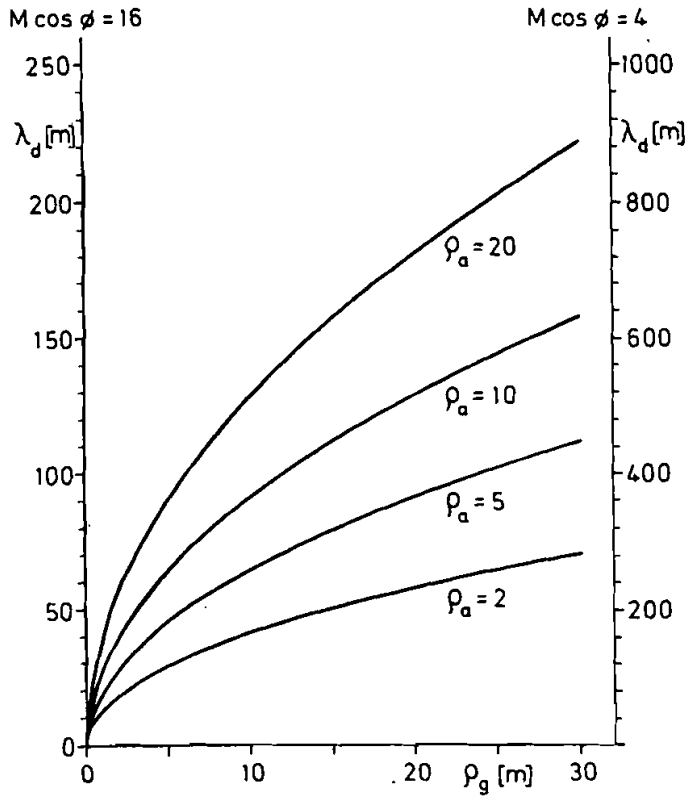

Figure 4. Dependence of clutter-limited detection cut-off wavelength $\lambda_d \equiv \lambda_d^{cl} = (k_d^{cl})^{-1}$ on the modulation factor $|M \cos \phi|$ and ground-range and aximuthal resolution scales ρ_g and ρ_a, respectively (equation (29)). The units of ρ_a are metres.

band), polarization: HH, θ (incidence angle) = 23°, $\rho_g = 35$ m, $\rho_a = 2{\cdot}6$ m (single look), n (number of looks) = 9, R (nine-look radiometric resolution) = 2·5 dB.

Since R is conventionally defined by (Brooks and Miller 1980)

$$R = \frac{\sigma_0 + n^{-1/2}(\sigma_0 + \sigma_0^{ne})}{\sigma_0} \tag{38}$$

the last statement implies

$$\frac{\sigma_0^{ne}}{\sigma_0} = 1{\cdot}33\ (1{\cdot}25\ \text{dB}) \tag{39}$$

Estimates of the sea return in C-band at 23° incidence angle and HH polarization vary from $\sigma_0 = -18$ db at low wind speeds in the cross-wind direction to $\sigma_0 = 10$ db at high wind speeds (Daley *et al.* 1968, 1969, 1970, 1971, 1973, Guinard and Daley 1970, Valenzuela *et al.* 1971, Guinard *et al.* 1971).

An optimal clutter-to-noise ratio of unity may be realized at very low wind speeds, but the SAR will again be operating in the clutter-limited regime at normal wind speeds (and, with allowance for system margin, probably at all wind speeds).

Substitution of these parameters in equation (34) yields:

$$(\lambda_d^{cl})_{ERS\text{-}1} \quad \frac{430}{|M \cos \phi|} \tag{40}$$

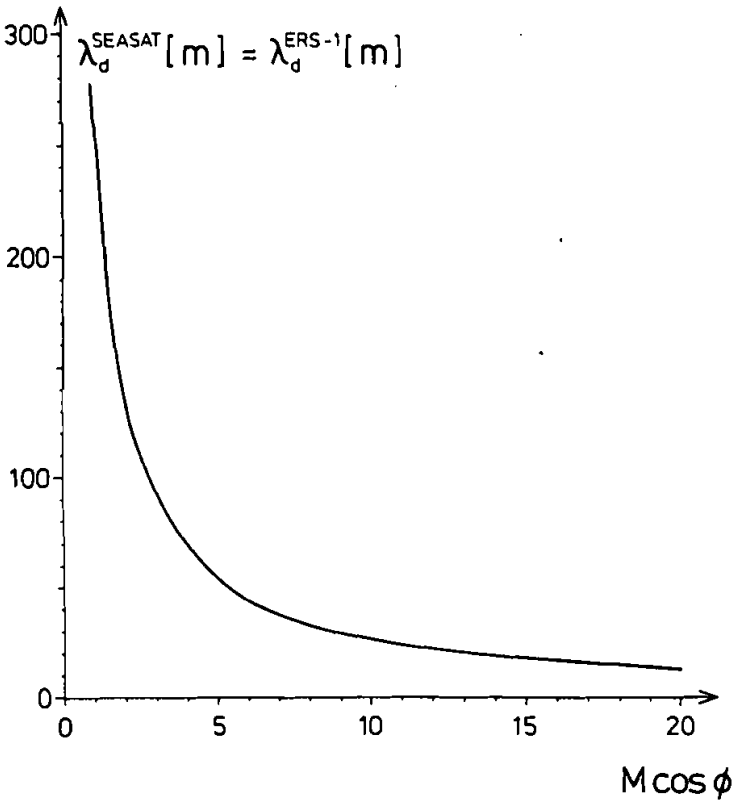

Figure 5. Dependence of detection cut-off wavelength $\lambda_d = k_d^{-1}$ on the modulation factor $|M\cos\phi|$ for Seasat and ERS-1.

which is of the same order of magnitude as the Seasat cut-off wavelength.

Appendix A

The clutter spectrum

The approximate scaling relation (19) for the clutter spectrum derived in §3 ignores the details of the SAR impulse response function and the filtering procedures required to estimate the variance spectrum for a finite-sized image. In the following we give a more complete analysis including these considerations. The analysis is essentially a specialization to a SAR of the general discussion of Fourier transforming radars given in Hasselmann and Alpers (1983).

The finite-resolution Fourier amplitude $\hat{A}(\mathbf{k})$ of a finite-area, single-look SAR image $I(\mathbf{x})$ is usually defined through an integral of the form

$$\hat{A}(\mathbf{k}) = \iint_{-\infty}^{\infty} d\mathbf{x} \exp(-2\pi i \mathbf{k}\mathbf{x}) I(\mathbf{x}) H(\mathbf{x})$$

or, denoting the Fourier transform operator $\iint d\mathbf{x} \exp(-2\pi i \mathbf{k}\mathbf{x})$ by the symbol $\hat{}$,

$$\hat{A} = \widehat{I \cdot H} \tag{A 1}$$

Here $H(\mathbf{x})$ represents an appropriately normalized tapering (window) function which is set identically zero outside the area of the scene. To avoid factors of 2π in the

convolutions occurring later, **k** is defined here as elsewhere in this paper in cycles per length rather than radians per length.

The finite-resolution variance spectrum is given by the expectation value, over the ensemble of long waves, of the square modulus of A,

$$E(\mathbf{k}) = |A(\mathbf{k})|^2 = (\widehat{I \cdot H})(\widehat{I \cdot H})^* \tag{A 2}$$

The clutter spectrum represents the difference between the expectation value $\langle E(\mathbf{k})\rangle$ of the variance spectrum of the image, averaged over the ensemble of small-scale scatterers (this clutter averaging can be assumed to be already included in the modulation-scale ensemble average in (A 2)) and the variance spectrum $E_{sig}(\mathbf{k})$ of the mean image, in which the averaging over the small-scale scatterers is assumed to have already been carried out before the image is Fourier transformed,

$$E_{cl}(\mathbf{k}) = \langle E(\mathbf{k})\rangle - E_{sig}(\mathbf{k}) \tag{A 3}$$

We consider first the signal variance spectrum $E_{sig}(\mathbf{k})$ of the clutter-averaged image. The scene considered may be regarded as a finite subsection of statistically homogeneous, infinite image whose Fourier components satisfy the orthogonality condition, with respect to wave-ensemble averages,

$$\overline{\hat{I}(\mathbf{k})\hat{I}^*(\mathbf{k}')} = \delta(\mathbf{k} - \mathbf{k}')E^{\infty}_{sig}(\mathbf{k}) \tag{A 4}$$

where $E^{\infty}_{sig}(\mathbf{k})$ denotes the infinite-resolution variance spectrum of the infinite image. (To simplify the notation we omit the clutter-average parentheses on $\hat{I}$ in (A 4) and later in (A 7)–(A 11).) Applying the convolution-Fourier transform commutation relations

$$\widehat{X \cdot Y} = \hat{X} * \hat{Y} \tag{A 5}$$

$$\widehat{X * Y} = \hat{X} \cdot \hat{Y} \tag{A 6}$$

where X, Y represent arbitrary functions, equation (A 2) may be written

$$E(\mathbf{k}) = [(\hat{I} * \hat{H})(\hat{I}^* * \hat{H}^*)] \tag{A 7}$$

and the relation (A 4) yields then for the finite-resolution signal spectrum the well-known relation

$$E_{sig}(\mathbf{k}) = E^{\infty}_{sig} * |\hat{H}|^2 \tag{A 8}$$

The infinite-resolution image signal spectrum E^{∞}_{sig} may be expressed in terms of the infinite-resolution variance spectrum E^{∞}_{σ} of the modulated cross-section distribution $\sigma_0(\mathbf{x})$ by applying (A 6) to (12),

$$\hat{I} = \hat{\sigma}_0 \cdot \widehat{|s|^2} \tag{A 9}$$

where s denotes the system impulse response function, and substituting (A 9) in (A 4),

$$E^{\infty}_{sig}(\mathbf{k}) = (\widehat{|s|^2})^2 \cdot E^{\infty}_{\sigma} \tag{A 10}$$

which yields, finally,

$$E_{sig}(\mathbf{k}) = [E^{\infty}_{\sigma} \cdot (\widehat{|s|^2})^2] * |\hat{H}|^2 \tag{A 11}$$

Turning now to the clutter spectrum, we can no longer base the analysis on quadratic moment expressions of the form (A 4), with respect to the real image field $I(\mathbf{x})$, since $I(\mathbf{x})$ itself depends quadratically on the complex backscattering coefficients

$r(\mathbf{x})$, which have not yet been clutter averaged. The clutter spectrum therefore requires the evaluation of fourth moments in $r(\mathbf{x})$ with respect to the ensemble of small-scale scatterers. Substitution of (11) and (12) into (A2) yields

$$E_{cl}(\mathbf{k}) = \langle E(\mathbf{k})\rangle - E_{sig}(\mathbf{k}) = \widehat{\langle((r*s)(r*s)^* \cdot H) \cdot ((r*s)(r*s)^* \cdot H)^*\rangle} - \widehat{(\langle(r*s)(r*s^*)\rangle \cdot H)(\langle(r*s)(r*s)^*\rangle \cdot H^*)} \tag{A 12}$$

Applying the analogous relation to (A 6) for the commutation of Fourier transforms and correlations,

$$\widehat{X \otimes Y^*} = \hat{X} \cdot \hat{Y}^* \tag{A 13}$$

where

$$X \otimes Y^* = X(\mathbf{x}) * Y^*(-\mathbf{x}) = \iint_{-\infty}^{\infty} X(\mathbf{x}+\mathbf{x}') \cdot Y^*(\mathbf{x}')\, d\mathbf{x}'$$

Equation (A 12) may be written

$$E_{cl}(\mathbf{k}) = \widehat{\langle((r*s)(r*s)^* \cdot H) \otimes ((r*s)(r*s)^* \cdot H^*)\rangle} - \widehat{(\langle(r*s)(r*s^*)\rangle \cdot H) \otimes (\langle(r*s)(r*s)^*\rangle \cdot H^*)} \tag{A 14}$$

The fourth moments occurring in the first term on the right-hand side of (A 14) may be expressed in terms of second moments using the relation

$$\langle \mu_1 \mu_2^* \mu_3 \mu_4^* \rangle = \langle \mu_1 \mu_2^* \rangle \langle \mu_3 \mu_4^* \rangle + \langle \mu_1 \mu_4^* \rangle \langle \mu_3 \mu_2^* \rangle \tag{A 15}$$

for complex, jointly Gaussian variables $\mu_1, \mu_2, \mu_3, \mu_4$. Substituting (A 15) into (A 14), one of the two combinations of second moments then cancels against the second term on the right-hand side of (A 14), and the remaining term yields

$$E_{cl}(\mathbf{k}) = \widehat{\int G^2(\mathbf{x}, \mathbf{x}') H(\mathbf{x}) H^*(\mathbf{x}+\mathbf{x}')\, d\mathbf{x}'} \tag{A 16}$$

where

$$G(\mathbf{x}, \mathbf{x}') = \int \sigma_0(\mathbf{x}'') s(\mathbf{x}' - \mathbf{x}'') s^*(\mathbf{x}+\mathbf{x}'+\mathbf{x}'')\, d\mathbf{x}'' \tag{A 17}$$

The expressions (A 16) and (A 17) simplify if $\sigma_0^2(\mathbf{x}'')$ can be regarded as approximately constant ($E_{cl} \approx E_{cl}^0$) in the integral in (A 17). One then obtains

$$G(\mathbf{x}, \mathbf{x}') \approx G(\mathbf{x}) = \sigma_0 s \otimes s^* \tag{A 18}$$

and

$$E_{cl}(\mathbf{k}) \approx \sigma_0^2 \widehat{(s \otimes s^*)(s^* \otimes s) \cdot (H \otimes H^*)} \tag{A 19}$$

Applying (A 5) and (A 13) this may be written in the alternative form

$$E_{cl}(\mathbf{k}) = \sigma_0^2 (|\hat{s}|^2 * \widehat{|s^*|^2} * |\hat{H}|^2) \tag{A 20}$$

Appendix B

The system noise spectrum—elementary scaling analysis

The main contributions to the system noise originate in the SAR receiver prior to amplification and the matched filtering in the processor. It is approximately white noise in the frequency band considered here and can be described by a system temperature T_n. In keeping with the elementary analysis of the clutter spectrum in §3,

we summarize in this appendix first the standard noise relations (see, for example, Skolnik 1970, chapter 2, or Hovanessian 1980) without entering into details of the system response functions or finite-resolution spectral filtering. The complete analysis including these considerations is given in Appendix C.

In order to express the thermal noise spectrum in the same cross-section units used to characterize the clutter and signal spectra in the elementary analysis of §3, we need to relate the system temperature T_n to the noise equivalent cross-section σ_0^{ne}. This is defined as the cross-section which yields the same energy per image pixel as the thermal noise.

The total noise power entering the SAR receiver is $W_n = kT_n B_r$, where k is Boltzmann's constant and B_r is the receiver bandwidth. This is normally matched to the bandwidth τ^{-1} of the emitted pulse, where τ is the pulse duration (after compression), so that $W_n = kT_n/\tau$. In the SAR processor, the signal corresponding to a given image pixel for a given pulse is gated for the time τ, so that the noise energy which is converted into a given image pixel for a single pulse is

$$\varepsilon_n^{(1)} = kT_n \tag{B 1}$$

The SAR processor sums over T_{int}/T_{pr} pulses, where T_{int} is the integration time and T_{pr} the pulse repetition interval, and since the noise is summed incoherently, the total noise energy per pixel is then

$$\varepsilon_n = kT_n \cdot T_{int}/T_{pr} \tag{B 2}$$

We compare this now with the energy received from a single resolution cell of area $\rho_a \cdot \rho_g$ and cross-section σ_0. According to the radar equation, the peak backscattered power W_r received by the radar for a single pulse is given by

$$W_r = W_e \eta^2 G_a^2 \frac{\lambda_0^2}{(4\pi)^3 r^4} \rho_a \rho_g \cdot \sigma_0 \tag{B 3}$$

where W_e denotes the peak power of the emitted pulse, r the range, λ_0 the radar wavelength, G_a the antenna gain and η the antenna efficiency. The gain G_a is related to the horizontal (azimuthal) and vertical antenna dimensions, D_h and D_v, by

$$G_a \approx 4\pi \frac{D_h}{\lambda_0} \cdot \frac{D_v}{\lambda_0} \tag{B 4}$$

and for an ideal SAR, ρ_a and D_h are related by

$$\rho_a = \frac{D_h}{2} \tag{B 5}$$

From (B 3) we may compute the energy received per pulse, $\varepsilon_r^1 = W_r \tau$, and the energy received through the coherent summation over T_{int}/T_{pr} pulses is then

$$\varepsilon_\sigma = W_r \cdot \tau \cdot (T_{int}/T_{pr})^2 \tag{B 6}$$

The noise equivalent cross-section is obtained by equating (B 2) and (B 6). Substituting (B 3) into (B 6) and replacing the peak emitted power by the mean power $\overline{W_e} = W_e \cdot \tau/T_{pr}$, one finds

$$\sigma_0^{ne} = \frac{kT_n}{\overline{W_e} \cdot T_{int}} \frac{(4\pi)^3 \cdot r^4}{\lambda_0^2} \frac{1}{G_a^2 \eta^2} \frac{1}{\rho_a \rho_g} \tag{B 7}$$

The integration time may be eliminated in equation (B 7) by using the relation for a full resolution (single-look) SAR

$$T_{\text{int}} = \frac{r\lambda_0}{2V\rho_a} \tag{B 8}$$

One obtains then, finally,

$$\sigma_0^{\text{ne}} = \frac{kT_n}{\overline{W_e}} \frac{2\cdot(4\pi)^3\cdot r^3\cdot V}{\eta^2 G_a^2 \lambda_0^3 \cdot \rho_g} \tag{B 9}$$

Appendix C

Thermal noise spectrum—detailed analysis

The thermal noise n_1 originating in the SAR receiver is a white-noise process whose covariance function is given by

$$\langle n_1^*(t+t')n_1(t)\rangle = \delta(t')kT_n \tag{C 1}$$

The cornered parentheses denote here averages over the ensemble of noise realizations. Equation (C 1) defines the system noise temperature T_n, assuming that n_1, which is proportional to the complex input voltage, is normalized such that $\langle|n|^2\rangle$ corresponds to the thermal noise input power (since n is an infinite bandwidth process, the input noise power $\langle|n|^2\rangle$ is infinite, but the output from a real finite bandwidth system remains finite).

The SAR processes the input signal using two time co-ordinates, the discrete azimuthal time t_a, which defined the emission times of individual pulses at the pulse repetition intervals T_{pr}, and the continuous t_r (which is limited, for non-ambiguous processing, to the interval $0 < t_r < T_{pr}$). In terms of those co-ordinates equation (C 1) may be written, with $n_1(t) \equiv n^d(t_a, t_r)$, as

$$\langle n^{d*}(t_a+t'_a, t_r+t'_r)n^d(t_a, t_r)\rangle = \delta^d(t'_a)\delta(t'_r)kT_n \tag{C 2}$$

where δ^d is the discrete δ-function

$$\delta^d(t'_a) = \begin{cases} 1 & \text{for } t'_a = 0 \\ 0 & \text{for } t'_a \neq 0 \end{cases}$$

The discrete complex image c_n^d generated by the thermal noise at the output of the linear SAR processor is given, as a function of the aximuthal and range-time co-ordinates, by a linear two-dimensional convolution of the form

$$c_n^d(t_a, t_r) = \sum_{t'_a} \int dt'_r \cdot s_n^d(t'_a, t'_r) n^d(t_a - t'_a, t_r - t'_r) \tag{C 3}$$

where s_n^d denotes the discrete system impulse response function for the thermal noise (which, as pointed out in §4, must be distinguished from the system signal input response function). Applying equation (C 2), the discrete mean real image $I_n^d(t_a, t_r)$ is then given by

$$I_n^d(t_a, t_r) = \langle|c_n^d(t_a, t_r)|^2\rangle = kT_n \sum_{t'_a} \int dt'_r |s_n^d(t'_a \cdot t'_r)|^2 \tag{C 4}$$

The elementary scaling relation (B 2) can be derived from (C 4) by substituting for the response function c_n^d the special case of a band-pass filter of width $1/\tau$ for the t_r-dependence and a unit-amplitude box-car function of width T_{int} for the t_a-dependence. Since $\int|s_n^d|^2\,dt_r = \int|\hat{s}_n^d|^2\,df = \tau^{-1}$, where $\hat{s}_n^d$ denotes the Fourier transform, we

obtain

$$\langle |c_n^d(t_a, t_r)|^2 \rangle = kT_n \cdot \tau^{-1} \cdot \left(\frac{T_{int}}{T_{pr}}\right) \tag{C 5}$$

The quantity $I_n^d = \langle |c_n^d(t_a, t_r)|^2 \rangle$ represents the image energy per unit range time for a given azimuthal line. The image noise energy per pixel is then

$$\varepsilon_n = I_n^d \cdot \tau = kT_n \cdot \left(\frac{T_{int}}{T_{pr}}\right) \tag{C 6}$$

in accordance with (B 2).

To determine the finite-resolution noise spectrum for an arbitrary noise impulse response function s_n^d, a fourth moment statistical analysis is required similar to the clutter analysis of Appendix A. Since the clutter and thermal noise statistics are, in fact, completely analogous, the results of Appendix A can be applied directly if equations (C 2) and (C 3) are rewritten in a continuous notation and the time variables are replaced by equivalent space variables in accordance with the relations

$$x_a = Vt_a$$

$$x_r = \frac{ct_r}{2}$$

In analogy with (8) and (11) we obtain then

$$\langle n^*(\mathbf{x}+\mathbf{x}')n(\mathbf{x})\rangle = kT_n \cdot \delta(\mathbf{x}') \tag{C 7}$$

$$c_n(\mathbf{x}) = \int s_n(\mathbf{x}')n(\mathbf{x}-\mathbf{x}')\,d\mathbf{x}' = s_n * n \tag{C 8}$$

where $n(\mathbf{x})$ denotes the continuous thermal noise function, $c_n(\mathbf{x})$ the continuous thermal noise complex image and $s_n(\mathbf{x})$ the continuous system impulse response function to thermal noise. Defining

$$s_n(x_a, x_r) \equiv s_n^d(t_a, t_r) \tag{C 9}$$

the normalization (C 7) follows from (C 8) and the normalization conditions between continuous and discrete functions

$$\left\langle \left(\iint_{x_a, x_r}^{x_a + \Delta x_a, x_r + \Delta x_r} n(\mathbf{x})\,dx_a\,dx_r \right)^2 \right\rangle = \left\langle \left(\sum_{t_a}^{t_a + \Delta t_a} \int_{t_r}^{t_r + \Delta t_r} n(t_a, t_r)\,dt_r \right)^2 \right\rangle \tag{C 10}$$

and

$$\langle |c_n|^2 \rangle \Delta x_a \Delta x_r = \langle |c_d|^2 \rangle \cdot \frac{\Delta t_a}{T_{pr}} \cdot \Delta t_r \tag{C 11}$$

which apply for arbitrary increments

$$\Delta x_a = V \cdot \Delta t_a \tag{C 12}$$

$$\Delta x_r = \frac{c}{2}\Delta t_r \tag{C 13}$$

The normalization (C 11) implies that in the continuous notation the mean real image $\langle I_n(\mathbf{x})\rangle = \langle |c_n|^2 \rangle$ is represented in units of received energy per unit area.

In analogy with (A 20), the thermal noise image variance spectrum is then given

by

$$E_n(\mathbf{k}) = (kT_n)^2 \cdot (|\hat{s}_n|^2 * |\widehat{s_n^*}|^2 * |\hat{H}|^2) \qquad \text{(C 14)}$$

It should be noted again that, in contrast to the thermal noise spectrum (25) and (26) derived in the elementary scaling analysis, the spectrum (C 14) refers to an image expressed in units of received energy, rather than cross-section units. Since the thermal noise impulse response function $s_n(\mathbf{x})$ differs from the signal impulse response function $s(\mathbf{x})$ entering in the clutter spectrum, it is not possible to relate the thermal noise spectrum directly to the clutter spectrum in terms of a noise equivalent cross-section, unless the analysis is reduced to the level of the elementary theory by introducing scaling arguments. To compare the clutter and thermal noise spectrum on the level of the exact analysis, it is therefore more convenient to express both the thermal noise spectrum and the clutter spectrum in terms of input power at the SAR receiver, using the radar equation and the system response structure outlined in figure C 1 (following Raney 1981).

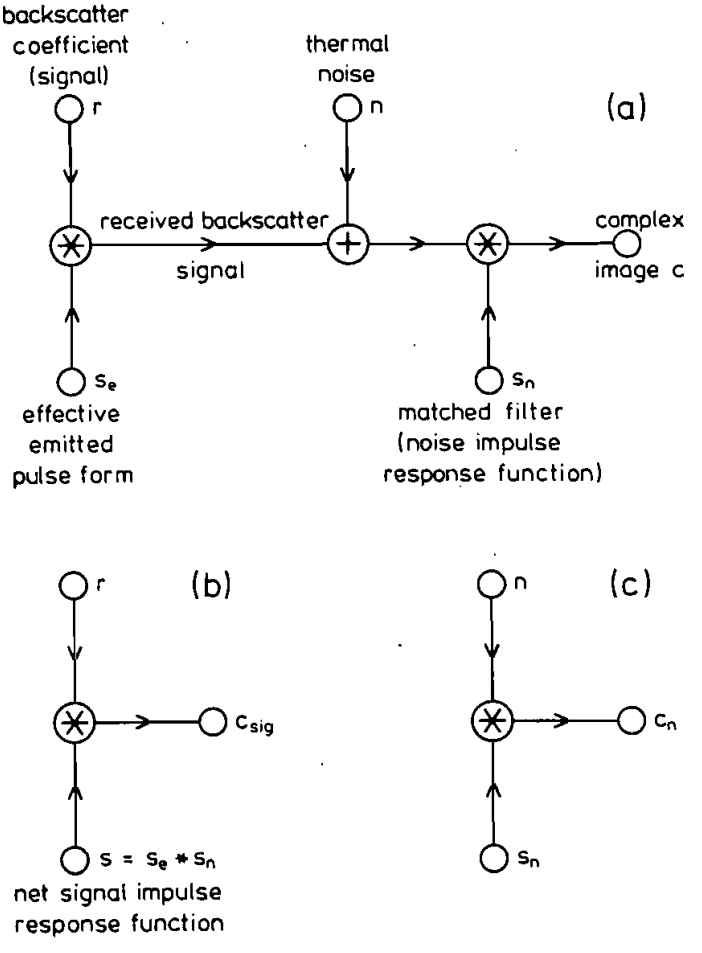

Figure C 1. SAR system response structure for (*a*) signal (backscatter coefficient) and noise, (*b*) signal alone and (*c*) noise alone. The effective emitted pulse form s_e consists of the product of the emitted pulse, an aximuthal phase factor, the square of the antenna gain pattern and geometric propagation factor (Hasselmann and Alpers 1983).

Appendix D

Multilook processing

The analysis of the paper has been carried through for a single-look, maximal resolution SAR processor. However, it can readily be shown that the results apply without significant modifications also for the multilook case. Within the approximations of the elementary scaling analysis (i.e. ignoring the details of the system response functions discussed in Appendixes A and C) the effects of the reduction in azimuthal integration time and receiver bandwidth associated with multilook aximuthal and range processing are exactly balanced by the accompanying increases in the azimuthal and range resolution scales, leaving the spectral levels of the clutter and thermal noise unchanged.

This can readily be seen by considering the effect of multilook processing on the statistics of individual pixels. If an image is formed by averaging n independent-look (real) images, the ratio of the mean square deviations $\overline{I'^2}$ of the multilook pixel energy to the square of the mean pixel energy $\overline{I}^2$ is reduced by a factor n^{-1} relative to the single-look case,

$$\left(\frac{\overline{I'^2}}{\overline{I}^2}\right)_{n\text{-look}} = \frac{1}{n}\left(\frac{\overline{I'^2}}{\overline{I}^2}\right)_{\text{single-look}} = \frac{1}{n} \tag{D 1}$$

This applies independently of the form of noise source for both clutter and thermal noise, and for both azimuthal and range multilook processing. Since the mean square fluctuations in pixel energy determine the total energy in the variance spectrum, this effect by itself would reduce the energy levels of the clutter and thermal noise spectra by a factor n^{-1}.

However, a change from single-look processing to n-look processing is accompanied by an increase in the area $\delta A = \rho_a \cdot \rho_g$ of the basic resolution cell by a factor n. Since the spectral density of the clutter noise, for given total variance of the spectrum, is inversely proportional to the bandwidth of the spectrum, i.e. proportional to the resolution cell area δA (see equation (19)), this increase of δA results in a corresponding increase in the clutter spectral density by a factor n.

Thus the reduction of the statistical fluctuation level by multilook averaging is compensated by the increase in resolution cell area, yielding a clutter noise spectral level which is independent of the number of looks.

The same conclusion also holds for the thermal noise spectrum. This can be deduced either from the formal analogy of the statistics of clutter and thermal noise shown in the full analyses of Appendices A and C, or, within the framework of the elementary scaling analysis of Appendix B, by generalizing the derivation of expression (26) ($\equiv$(B 9)) for the thermal noise equivalent cross-section to the multilook case.

In the case of azimuthal multilook processing one finds first that the thermal noise energy of a processed individual look at a given discrete image azimuthal time point is reduced by a factor n_a^{-1}, where n_a is the number of azimuthal looks, as a result of the reduced azimuthal integration time $(T_{\text{int}})_{\text{multilook}} = (T_{\text{int}})_{\text{single look}}/n_a$. However, this is compensated for on summing the energies of n_a independent looks, yielding the same thermal energy per azimuthal image time point as in the single-look case. The energy per pixel, containing n_a azimuthal time points, is then n_a times the energy of the (correspondingly smaller) single-look pixel. Similarly, the backscattered return from a given surface area for a given azimuthal time point is decreased by the factor n_a^{-1} due to the reduction in the number of coherent looks, but this is compensated by the

increase in the area of the basic resolution by the factor n_a, yielding again the same backscattered energy per azimuthal time point as in the single-look case. The energy per pixel is then n_a times the energy of the single-look pixel. Thus the noise equivalent cross-section, which is defined as the cross-section, which yields the same mean backscattered return as the thermal noise, remains the same in the multilook case as in the single-look case.

In the range direction, the extraction of n_r separate looks from a single emitted stretched pulse allows a reduction in the receiver bandwidth for each individual look by a factor n_r^{-1}. In computing the thermal noise energy received per pixel per individual look, this is then compensated by the increase in the duration of the signal corresponding to a given pixel, which is proportional to the ground range resolution $(\rho_g)_{\text{multilook}} = n_r(\rho_g)_{\text{single-look}}$. The summation over n_r separate looks then yields a net thermal noise energy per pixel which is n_r times the energy of the (correspondingly smaller) single-look pixel. For the backscattered return from the sea surface one finds, similarly, first a reduction in the received energy per individual look per unit surface area by a factor n_r^{-1} due to the subdivision of the received pulse into short subsections which are able to pass through the selective individual-look matched filters. This is then compensated again by summing over the n_r separate looks. Finally, the multilook backscatter energy per pixel must be multiplied by a factor n_r due to the increase in the surface area of the backscattering elementary resolution cell. Thus the ratio of the thermal energy to the backscatter energy per pixel, which determines the thermal noise equivalent cross-section, is also not affected by multilook processing in the range co-ordinate.

Since neither azimuthal nor range multilook processing influence the thermal noise equivalent cross-section, it follows that the clutter noise and thermal noise statistics follow the same scaling laws with respect to multilook processing. Thus if the clutter spectral level remains constant, the thermal noise spectral level must also remain constant. Thus the only effect of multilook processing is to reduce the Nyquist cut-off wavenumbers $k_N^a = (2\rho_a)^{-1}$, $k_N^g = (2\rho_g)^{-1}$ of the clutter and thermal noise spectra through the increase in the azimuthal and/or ground range resolution scales ρ_a, ρ_g. Multilook processing is thus seen to be essentially equivalent to single-look processing with subsequent averaging over n image pixels. Provided the Nyquist wavenumber components of the smoothed image remain greater than the signal-to-background detection cut-off wavenumber components k_d^a, k_d^g, the single-look analysis remains valid.

It may be noted in conclusion that although it is instructive to discuss the effects of multilook processing on the individual signal processing stages using scaling arguments, in the present case the invariance of the basic results of the single-look spectral clutter and thermal noise analysis with respect to multilook processing can be recognized more easily formally by direct inspection of the exact relations (22) and (27). The reduction in the two-dimensional bandwidths of the signal and noise impulse response functions in the quadratic convolutions occurring in (22) and (27) by a factor n is immediately seen to reduce the spectral levels for individual-look processing by a factor n, which is then just compensated by summing over n individual looks.

References

ALPERS, W. R., and HASSELMANN, K., 1978, The two-frequency microwave technique for measuring ocean wave spectra from an airplane or satellite. *Boundary Layer Meteorol.*, 13, 215.

ALPERS, W. R., ROSS, D. B., and RUFENACH, C. L., 1981, On the detectability of ocean surface waves by real synthetic aperture radar. *J. Geophys. Res.*, **86**, 6481.

ALPERS, W. R., and RUFENACH, C. L., 1979, The effect of orbital motions on synthetic aperature radar imaging of ocean waves. *I.E.E.E. Trans. Antennas Propag.*, **27**, 685.

BASS, F. G., FUKS, I. M., KALINYKOV, A. I., OSTROWSKY, I. E., and ROSENBERG, A. D., 1968, Very high frequency radio wave scattering by a disturbed sea surface. *I.E.E.E. Trans. Antennas Propag.*, **16**, 554.

BEAL, R., SPRINGETT, J., LIPES, R., WU, C., and EVANS, N., 1977, Seasat-A SAR design verification report. Report 622–31, Jet Propulsion Laboratory, Pasadena, California.

BROOKS, S. R., and MILLER, P. F., 1980, The influence of radiometric resolution on synthetic aperture radar design parameters. In *Seasat-SAR Processor* (Proceedings of an ESA workshop held in Frascati, 10–14 December 1979) (Noordwijk: ESA Scientific and Technical Publication Branch, ESTEC), ESA-SP 154, pp. 25–30.

DALEY, J. C., DAVIS, W. T., and MILLS, N. R., 1970, Radar sea return in high sea states. Report No. 7142, Naval Research Laboratory, Washington, D.C.

DALEY, J. C., RANSONE, J. T., and BURKETT, J. A., 1971, Radar sea return—JOSS I. Report No. 7268, Naval Research Laboratory, Washington, D.C.

DALEY, J. C., RANSONE, J. T., BURKETT, J. A., and DUNCAN, J. R., 1968, Sea-clutter measurements on four frequencies. Report No. 6806, Naval Research Laboratory, Washington, D.C.

DALEY, J. C., RANSONE, J. T., BURKETT, J. A., and DUNCAN, J. R., 1969, Upwind-downwind-crosswind sea clutter measurements. Report No. 6881. Naval Research Laboratory, Washington, D.C.

DALEY, J. C., RANSONE, J. T., and DAVIS, W. T., 1973, Radar sea return—JOSS II. Report No. 7534, Naval Research Laboratory, Washington, D.C.

DORNIER, 1980, Satellite scatterometer feasibility study. Final Report, ESA Contract No. 4367/80/F/DD (SC), Technical Results, ESA Contract No. 4656/81/F/DD (SC).

GUINARD, N. W., and DALEY, J. C., 1970, An experimental study of a sea clutter model. *Proc. I.E.E.E.*, **58**, 543.

GUINARD, N. W., RANSONE, J. T., and DALEY, J. C., 1971, The variation of the radar cross-section of the sea with increasing roughness. *J. Geophys. Res.*, **76**, 1525.

HASSELMANN, K., 1980, A simple algorithm for the direct extraction of the two-dimensional surface image spectrum from the return signal of a synthetic aperture radar. *Int. J. remote Sensing*, **1**, 219.

HASSELMANN, K., and ALPERS, W., 1983, Fourier transforming radars. (In preparation.)

HOVANESSIAN, S. A., 1980, Introduction to synthetic array and imaging radars. Artech House, Inc., Dedham, Massachusetts.

JACKSON, F. C., 1980, An analysis of short pulse and dual frequency radar techniques for measuring ocean wave spectra. NASA Technical Memorandum 82011, Goddard Space Flight Center, Greenbelt, Maryland.

JENKINS, G. M. and WATTS, D. G., 1968, *Spectral Analysis and its Application*, (San Francisco: Holden-Day), 525 pp.

JORDAN, R. L., 1980, The Seasat-A synthetic aperture radar system. *I.E.E.E. Jl oceanic Engng*, **5**, 154.

KASISCHKE, E. S., 1980, Extraction of gravity wave information from spaceborne synthetic aperture radar data. M. Sc. Thesis, University of Michigan, Ann Arbor, Michigan.

KELLER, W. C., and WRIGHT, J. W., 1975, Microwave scattering and straining of wind generated waves. *Radio Sci.*, **10**, 139.

MCLEISH, W., ROSS, D., SHUCHMAN, R. A., TELEKI, P. G., HSIAO, S. V., SHEMDIN, O. H., and BROWN, W. E., 1980, Synthetic aperture radar imaging of ocean waves: comparison with wave measurements, *J. geophys. Res.*, **85**, 5003.

MARTIN, P., 1981, Direct determination of the two-dimensional image spectrum from raw synthetic aperature radar data. *I.E.E.E. Trans. Geosci. remote Sensing* (in the press).

PHILLIPS, O. M., 1977, *The Dynamics of the Upper Ocean* 2nd edn. New York: Cambridge University Press).

PLANT, W. J., 1977, Studies of backscattered sea return with CW dual-frequency, X-band radar. *I.E.E.E. Trans. Antennas Propag.*, **25**, 28.

RANEY, R. K., 1981, Wave orbital velocity, fade, and SAR response to azimuth waves. *I.E.E.E. Jl Oceanic Engng* (in the press).

RUFENACH, C. L., and ALPERS, W., 1981, Imaging ocean waves by synthetic aperture radars with long integration times. *I.E.E.E. Trans. Antennas Propag.*, **29**, 422.

SKOLNIK, M. I. (editor), 1970, *Radar Handbook* (New York: McGraw-Hill).

SWIFT, C. T., and WILSON, O. R., 1979, Synthetic aperture radar imaging of ocean waves. *I.E.E.E. Trans. Antennas Propag.*, **27**, 725.

VALENZUELA, G. R., 1980, An asymptotic formulation for SAR images of the dynamical ocean surface. *Radio Sci.* **15**, 105.

VALENZUELA, G. R., LAING, M. B., and DALEY, J. C., 1971, Ocean spectra for the high-frequency waves as determined from airborne radar measurements, *J. Mar. Res.*, **29**, 69.

VESECKI, J. F., and STEWART, R. H., 1982, The observation of ocean surface phenomena using imagery from the Seasat synthetic aperture radar—an assessment. *J. geophys. Res.*, **87**, 3397.

WRIGHT, J. W., 1968, A new model for sea clutter. *I.E.E.E. Trans Antennas Propag.*, **16**, 217.

WRIGHT, J. W., PLANT, W. J., KELLER, W. C., and JONES, W. L., 1980, Ocean wave-radar modulation transfer functions from the West Coast Experiment. *J. geophys. Res.*, **85**, 4957.